1   **Surface Dimming by the 2013 Rim Fire Simulated by a Sectional Aerosol Model**

2   Pengfei Yu[1,2,3,4], Owen B. Toon[1,2], Charles G. Bardeen[5], Anthony Bucholtz[6], Karen H.

3   Rosenlof[4], Pablo E. Saide[5,7], Arlindo Da Silva[11], Luke D. Ziemba[8], Kenneth L.

4   Thornhill[9], Jose-Luis Jimenez[10,3], Pedro Campuzano-Jost[10,3], Joshua P. Schwarz[3,4], Anne

5   E. Perring[3,4], Karl D. Froyd[3,4], N. L. Wagner[3,4], Michael J. Mills[5] and Jeffrey S. Reid[6],

6   [1] Laboratory for Atmospheric and Space Physics, University of Colorado, Boulder, CO,

7   USA

8   [2] Department of Atmospheric and Oceanic Sciences, University of Colorado, Boulder,

9   CO, USA

10   [3] Cooperative Institute for Research in Environmental Science, University of Colorado,

11   Boulder, CO, USA

12   [4] Earth System Research Laboratory, National Oceanic and Atmospheric Administration,

13   Boulder, CO, USA

14   [5] Atmospheric Chemistry Observations and Modeling Laboratory, National Center for

15   Atmospheric Research, Boulder, CO, USA

16   [6] Naval Research Laboratory, Monterey, CA, USA

17   [7] Center for Global & Regional Environmental Research, The University of Iowa, Iowa,

18   USA

19   [8] NASA Langley Research Center, Hampton, VA, USA

20   [9] Science Systems and Applications, Inc., Hampton, VA, USA.

21   [10] Department of Chemistry and Biochemistry, University of Colorado, Boulder, CO,

22   USA.

23   [11] NASA Goddard Space Flight Center, Greenbelt, MD, USA.

24 **Key Points**

25 • The Rim Fire of 2013 is simulated by a size-resolved aerosol model within the CESM

26   model.

27 • Simulated aerosol properties are within data variability.

28 • Rim Fire smoke cooled the surface by 120-150 Wm^{-2} per unit mid-visible AOD at

29   13:00-15:00 local time.

30 **Abstract**

31 The Rim Fire of 2013, the third largest area burned by fire recorded in California history,

32 is simulated by a climate model coupled with a size-resolved aerosol model. Modeled

33 aerosol mass, number and particle size distribution are within variability of data obtained

34 from multiple airborne *in-situ* measurements. Simulations suggest Rim Fire smoke may

35 block 4-6% of sunlight energy reaching the surface, with a dimming efficiency around

36 120-150 W m^{-2} per unit aerosol optical depth in the mid-visible at 13:00-15:00 local time.

37 Underestimation of simulated smoke single scattering albedo at mid-visible by 0.04

38 suggests the model overestimates either the particle size or the absorption due to black

39 carbon. This study shows that exceptional events like the 2013 Rim Fire can be simulated

40 by a climate model with one-degree resolution with overall good skill, though that

41 resolution is still not sufficient to resolve the smoke peak near the source region.

1. Introduction

Forest fire smoke can cool the planet in the daytime by scattering sunlight [*Robock,* 1988; *Robock,* 1991; *Westphal and Toon,* 1991]. *Robock* [1991] used the difference between forecasted and observed temperatures to suggest that forest fires in Canada during 1981 and 1982, Siberia in 1987, as well as in Yellowstone National Park in 1988, cooled the surface under the smoke by 1.5 to 7 °C in the daytime, but did not have an observable impact on nighttime temperatures. Using a numerical model, *Westphal and Toon* [1991] found a daytime cooling of 5 °C beneath a smoke plume over the Northeastern U.S., which originated from a fire in Western Canada in 1982.

The Rim Fire of 2013 burned the third largest area recorded in California history. The fire, located near Yosemite National Park, lasted from August to October [*Peterson et al.*, 2015]. This exceptional event provides a good opportunity to further quantify radiative forcing by forest fires using modern global climate modeling approaches constrained by both remote and *in-situ* data. The Rim Fire started on August 17 and spread rapidly until August 31, 2013 due to warm ambient temperatures, high near-surface wind speeds and low relative humidity [*Peterson et al.*, 2015]. NASA's Studies of Emissions and Atmospheric Composition, Clouds and Climate Coupling by Regional Surveys field program (SEAC[4]RS, Toon et al. [2016]) sampled the Rim Fire smoke on August 26 and August 27. Multiple instruments on board the NASA DC-8 aircraft provide a unique and rich dataset on aerosol properties and chemical tracers in Rim Fire smoke.

We use a climate model coupled with a size-resolved aerosol model to simulate the Rim Fire smoke in order to examine if a relatively low-resolution model can correctly

65   reproduce the physical and optical properties of Rim Fire smoke. In section 2 we

66   introduce the detailed modeling settings and emissions sources used; in section 3 we

67   summarized observational datasets used in the study; in section 4 we evaluate the model

68   performance on Rim Fire simulations; in section 5 we discuss the radiative impacts of

69   Rim Fire smoke simulated by model; in section 6, we summarize the main findings of

70   this study.

71   **2. Model Settings and Study Region**

72   Physical and optical properties of Rim Fire smoke are simulated using the

73   Community Earth System Model, version 1, CESM1, coupled with a sectional aerosol

74   microphysics model, the Community Aerosol and Radiation Model for Atmospheres

75   (CARMA) [*Toon et al.,* 1988; *Yu et al.,* 2015a]. Our version of CESM1/CARMA

76   includes two groups of particles. The first group is composed of liquid droplets of

77   sulfuric acid that have nucleated from the gas phase. The second group is an internal

78   mixture of primary emitted organics, secondary organics, dust, sea salt, black carbon and

79   condensed sulfate. Ammonia or nitrate is currently not included in CARMA. To compare

80   with field observations, we extract the nearest model grid-box output (1.9°x2.5°, 30

81   minutes for time-step) along the flight track spatially and temporally.

82   Aerosol optical properties are calculated using Mie scattering theory. For the

83   internally mixed particles a core shell structure is assumed. The core is composed of

84   black carbon and dust, while the shell is composed of materials that are possibly in a

85   liquid state including sulfate, organics, salt and condensed water. At mid-visible

86   wavelengths, the refractive index of black carbon is assumed to be 1.75-0.443i and the

87   index of the shell is assumed to be 1.43+0i according to *Hess* et al. [1998]. Absorption of

88　brown carbon [*Forrister et al.,* 2015] is currently not modeled. Aerosol optical properties

89　(scattering coefficient, absorption coefficient, single scattering albedo, asymmetry

90　parameter) are passed to CESM1's RRTMG radiation model [*Iacono et al.,* 2008] for

91　online radiative calculation of forcing and heating rates. The optical properties vary

92　spatially and temporally with dry particle size, relative humidity, black carbon amount

93　and dust amount [*Yu et al*., 2015a].

94　　Details of CESM/CARMA are described in *Yu et al.* [2015]. To better resolve the

95　Rim Fire smoke, we conducted runs with one-degree horizontal resolution instead of the

96　2-degree resolution used in *Yu et al.* [2015]. Simulations were run for five years (from

97　2007 to 2012) to spin-up the aerosol and chemical tracers. The Rim Fire smoke was

98　introduced in the 6th year of the model run (i.e. year 2013).

99　　Runs were nudged to offline meteorology (temperature and winds) using data from

100　the Modern Era Retrospective-Analysis for Research, MERRA, [*Rienecker et al.,* 2011]

101　for the SEAC^{4}RS period. The nudging relaxes the model towards MERRA temperature

102　and winds by 1% each time step (i.e. 30 minutes). Sea surface temperature (SST) is

103　prescribed. The biomass burning emissions are determined using the daily Quick Fire

104　Emission Dataset (QFED, *Darmenov and da Silva,* [2014]). Emissions are tabulated in

105　the QFED at 0.1-degree resolution, which we re-grid to the model resolution of 1 degree.

106　QFED emissions for rim fires are evaluated and found not sufficient to resolve observed

107　smoke amount [*Saide et al*., 2015]. We applied the correction factors generated by *Saide*

108　*et al.* [2015] for daily Rim Fire Emissions (37.75 to 38.15°N and 120.3 to 119.05°W)

109　from Aug.21 to Aug.27. Anthropogenic emissions of organics and black carbon come

110　from *Amann et al.* [2011]. Table 1 lists the adjusted daily biomass burning emission rate

111   (g/m^2/day) for organic aerosol (OA) and black carbon for the Rim Fire. The ratio of the

112   daily emissions of OA to BC ranges from about 26 to 36.

113   Table 1 Adjusted Emission Rate (kg s^{-1} m^{-2}) between 37.75 to 38.15°N and 120.3 to

114   119.05°W

Emission	BC	OA	OA/BC
Aug.21	2.01E-09	6.68E-08	33.2
Aug.22	3.60E-09	9.45E-08	26.3
Aug.23	4.89E-10	1.46E-08	29.8
Aug.24	3.58E-10	1.23E-08	34.5
Aug.25	1.42E-10	4.83E-09	34.1
Aug.26	2.83E-10	9.81E-09	34.6
Aug.27	2.12E-10	7.00E-09	33.0
Aug.28	9.67E-11	3.34E-09	34.6
Aug.29	1.01E-10	3.37E-09	33.3
Aug.30	3.13E-11	1.12E-09	35.7
Aug.31	1.20E-11	4.29E-10	35.8

115

116   The injection height of Rim Fire smoke measured by DIAL/HSRL was 3-5 km

117   above the ground, which is roughly between 700 to 500 hPa [*Peterson et al.,* 2015]. We

118   put the Rim Fire emissions at five pressure levels of CESM between 712 and 581 hPa,

119   with a peak at 618 hPa. Note the injection height used in the model remains constant with

120   time. The emissions are vertically distributed in a Gaussian distribution with a median

121   injection height at 618 hPa and a width of 25 hPa. The peak location (around 618 hPa) is

122   consistent with the location of the highest measured organic concentration along the Rim

123   Fire smoke plumes. We also examined an alternative approaches to inject the smoke near

124   surface or higher than the observed smoke peak, and we found modeled smoke matches

125   observation the best when we inject the smoke near 618 hPa.

126   The modeled particle size distribution is controlled by the size distribution at time

127   of emission, particle microphysical process (e.g. coagulation, growth, evaporation and

128   deposition), and condensation of water. The initial particle size distribution for smoke

129   emissions is based on a daily mean size distribution retrieved by AERONET at

130   University of Nevada-Reno on Aug.26 of 2013 when Rim fire smoke heavily impacted

131   the site.

132   The model outputs aerosol mass, number, compositions, size and optical

133   properties along the DC8 flight track (shown in Figure 1) when and where the

134   measurements are taken. Model's spatial ($0.9°$x$1.25°$) and temporal (30 min) resolution is

135   lower than reported observational resolution (1 Hz, about 200 m). Simulated aerosol

136   fields are interpolated using the nearest four model grid points and closest time step

137   where and when the measurements are taken.

138   **3.   Observational datasets**

139   Details of observational datasets on board of DC8 are documented in Table 4 of

140   *Toon et al.* [2016]. Table 2 lists aerosol properties used in this study and basic

141   information of their instruments.

142   Table 2 Aerosol properties and instruments used in this study

Properties	Instruments	References
BC	HD-SP2	Schwarz et al., 2013
OM	HR-AMS	Dunlea et al., 2009
ND	LARGE*LAS	
Area	LARGE*LAS	
Volume	LARGE*LAS	
Extinction	LARGE Nephelometer	Chen et al., 2011
Extinction	CRDS	Langridge et al., 2011
Dust	PALMS	Murphy et al., 2006
AOD	MODIS	Sayer et al., 2013

143   Note: *LAS denotes TSI Laser Aerosol Spectrometer.

144   **4.   Comparing Simulations with Observations of Rim Fire Smoke**

145   Figure 1 shows the measured concentration of sub-micron OA along the flight

146   tracks of the DC-8 on 8/26 and on 8/27 as measured by the Aerosol Mass Spectrometer

147   (AMS) [*Dunlea et al.*, 2009, 0.1 to 1 μm in diameter]. In this paper we consider the

148   smoke from California to Montana with the highest concentrations OA, (red dashed circle

149   in Figure 1) as the region of the smoke cloud, because it is most likely to have observable

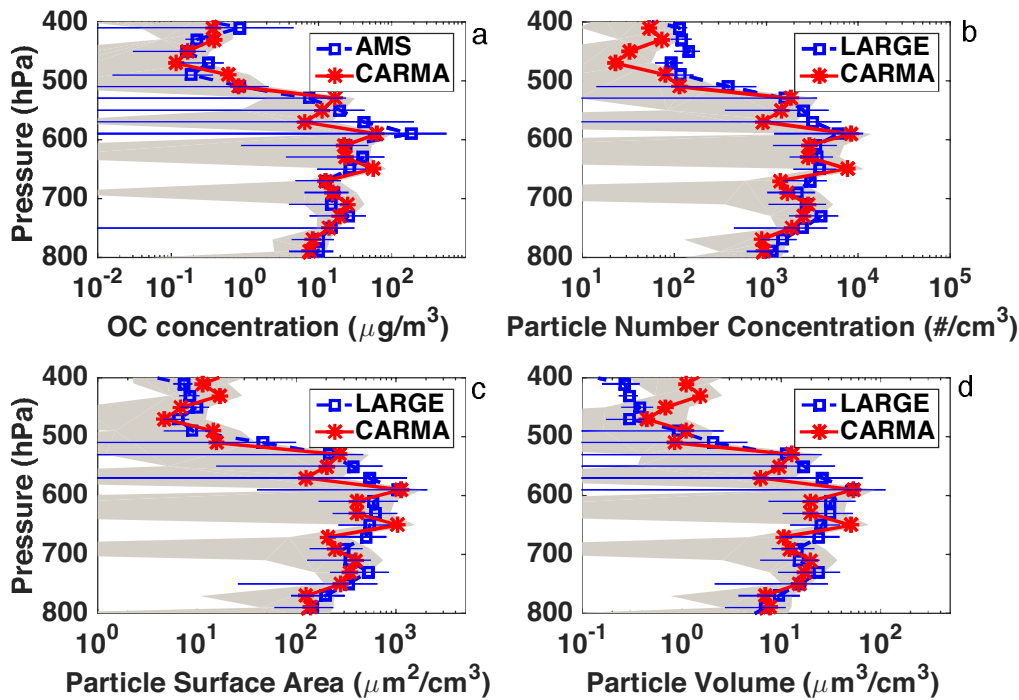150   radiative effects due to its large aerosol concentration.

151

Figure 1 Concentration of OA in standard air (unit: μg/std m^3) along the flight tracks of

153   the DC-8 from 8/26 to 8/27. Study region is marked by red dashed circle. Starting points

154   of flight of 8/26 and 8/27 are denoted by the black text arrows.

155   Figure 2 shows various aerosol properties in Rim Fire smoke observed by the

156   AMS, and the Langley Aerosol Research Group Experiment (LARGE, 0.1 to 6.3 μm in

157   diameter), and as simulated by CESM/CARMA using the same aerosol size ranges. Both

158   model and observations suggest the effective radius (around 0.14 μm, measured by

159   LARGE laser aerosol spectrometer) of smoke particles remains constant downwind,

160   which is not shown in the figures in this paper. However, the lack of change in effective

161   radius does suggest that no significant conversion of secondary organic aerosol or other

162   gases to aerosols occurred as the smoke moved downwind. In addition observed

163   Angstrom exponent (AE) of scattering (450 nm to 550 nm) from LARGE remains

164   constantly along the smoke (ranging from 1.9 to 2.2, AE is derived from scattering

165   coefficients measured by Nephelometers). The smoke simulated in the model remains

166   constant in altitude with limited variation, not much diurnal variations are shown in the

167   model. Smoke does sink or dissipate in the model following winds. The simulated OA

168   mass concentration, particle number concentration, surface area concentration and

169   volume concentration in standard air averaged along the flight track within the dashed

170   circle in Figure 1, are within data variability (one standard deviation). Generally the OA

171   concentration from Rim Fire smoke peaks at around 600 hPa and decreases sharply by 2-

172   3 orders of magnitude up to 400 hPa. The OA concentrations also decrease by 1 order of

173   magnitude between 600 and 800 hPa. The mean of the simulated OA concentration, and

174   the other particle concentrations, are lower than the mean observed between 550 to 600

175   hPa, though they are still within the variability. It is possible that the concentrations are

176   low because the 1-degree model is not able to resolve sub-grid smoke plumes near the

177   source region. It is also possible that the initial injection profile assumed from 700 to 500

178   hPa with a peak at 600 hPa, is not completely correct. The large spatial and temporal

179   variabilities of smoke (observed and modeled) shown in Figure 2 is partly because the

180   aircraft is occasionally flying above or outside the smoke plume.

181

Figure 2 OA concentration (a), particle number density (b), aerosol surface area density

(c) and aerosol volume density (d) of standard air simulated by CARMA (shown in solid

red lines) and observed in SEAC[4]RS (show in dashed blue lines). Error bars denote

variability (one standard deviation) of observations. Grey shadings denote temporal and

spatial variability of the model (one standard deviation). Data are averaged from

California to Montana along the flight track inside the dashed circle in Figure 1.

Figure 3 shows aerosol extinction along Rim Fire smoke observed by LARGE (in

blue dashed line, Chen et al. [2011]) and NOAA Aerosol cavity ringdown extinction

spectrometer (in green dashed line, Langridge et al. [2011]), and modeled by CARMA (in

red solid line). Error bars denote one standard deviation of data. As shown in Figure 3 the

model underestimates the aerosol extinction coefficient in the smoke region between 550

and 650 hPa. The extinction coefficient is measured as the sum of scattering and

absorption coefficients. Scattering is measured with dual integrating nephelometers

195   operating at less than 40% and 80% relative humidity so that the extinctions are adjusted

196   to the ambient humidity [*Ziemba et al.* 2013]. Absorption is measured by a particle soot

197   absorption photometer. For the region below 650 hPa, the simulations are within the

198   variability of the observations.

199   The comparisons in Figure 2 and Figure 3 suggest CESM/CARMA generally

200   captures the location and physical properties of Rim Fire smoke, although the simulations

201   may underestimate concentrations. The underestimation may be a consequence of the 1-

202   degree resolution being inadequate to fully capture the denser parts of the smoke plume.

203   Alternatively, the daily-averaged input emissions (without diurnal cycle) may be an

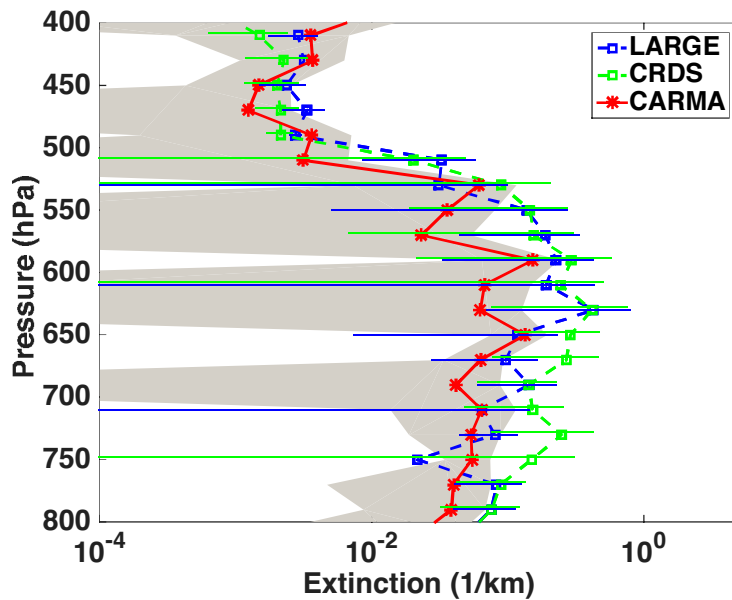204   underestimate.

205

206   Figure 3 Extinction coefficients at mid-visible wavelength simulated by CARMA (red)

207   and observed by LARGE (blue), CRDS (green). Error bars denote data variability (one

208   standard deviation) of observations. Grey shading denotes temporal and spatial variability

209   of model (one standard deviation).

210   Figure 4 (left panel) illustrates the OA to BC mass ratio as a function of altitude

211   simulated by CARMA (in solid red line) and calculated based on observational datasets

212   (in dashed blue line). Both model and observation suggest the ratio of OA to BC is quite

213   large in the Rim Fire smoke. The data suggests the ratio is about 40-60, and the model

214   about 30-40 for pressures higher than 550 hPa. Table 1 shows that the emission of

215   primary OA from the fire is assumed to be 26-36 times that of black carbon. *Forrister et*

216   *al.* [2015] showed that no net Secondary Organic Aerosol formation was observed in the

217   Rim Fire plume, consistent with observations for most other wildfire plumes studied from

218   aircraft [*Cubison et al.*, 2011; *Jolleys et al.*, 2012]. The comparison thus suggests that the

219   initial injected OA-to-BC ratio may be too low.

220   Figure 4 (right panel) compares the simulated SSA in the Rim Fire smoke (0.91)

221   with two sets of observations: one is humidified particle SSA measured by LARGE

222   [*Ziemba et al*., 2013], the other one is dry particle SSA measured by a combination of

223   CRDS (measure dry extinction coefficient) and NOAA Aerosol photo-acoustic

224   absorption spectrometer (PAS, measure dry absorption coefficient). Both measured SSA

225   values are about 0.95 in the smoke region between 550 hPa and 700 hPa, which is larger

226   than the modeled value (0.91). As shown previously, we chose a relatively low value of

227   the imaginary refractive index for BC, and we did not consider any absorption by Brown

228   Carbon, which was present in this fire [*Forrister et al.,* 2015]. Both of these assumptions

229   could bias the single scattering albedo high, rather than low as indicated by the

230   observations. The single scattering albedo is likely too low in our simulations because the

231   ratio of organic carbon to black carbon is about 25% too low, but larger particles could

232   also reduce the SSA.

233   The observed OA-to-BC ratio declines above the Rim Fire smoke for pressures

234 less than 550 hPa**.** The simulated ratio also declines to about 10, and as a consequence the

235 simulated single scattering albedo (SSA) at mid-visible declines for pressures less than

236 550 hPa. Using combined measurements of CRDS and PAS, the observed SSA declines

237 as low as 0.5 at 430 hPa (not shown in Figure 4). However measured absorption

238 coefficients above 500 hPa are close to the detection limit of PAS (2×10^{-3} km^{-1}). The

239 lower SSA values at pressures below 550 hPa are partly due to the lower OA to BC ratio

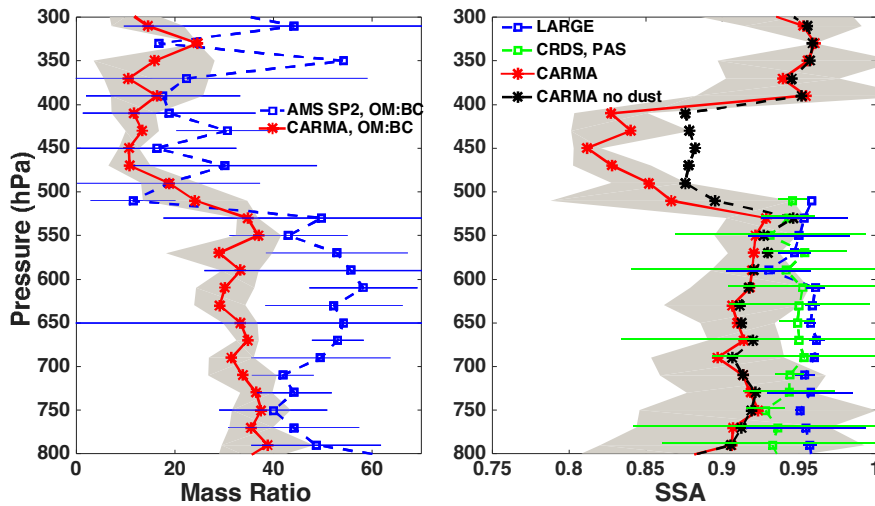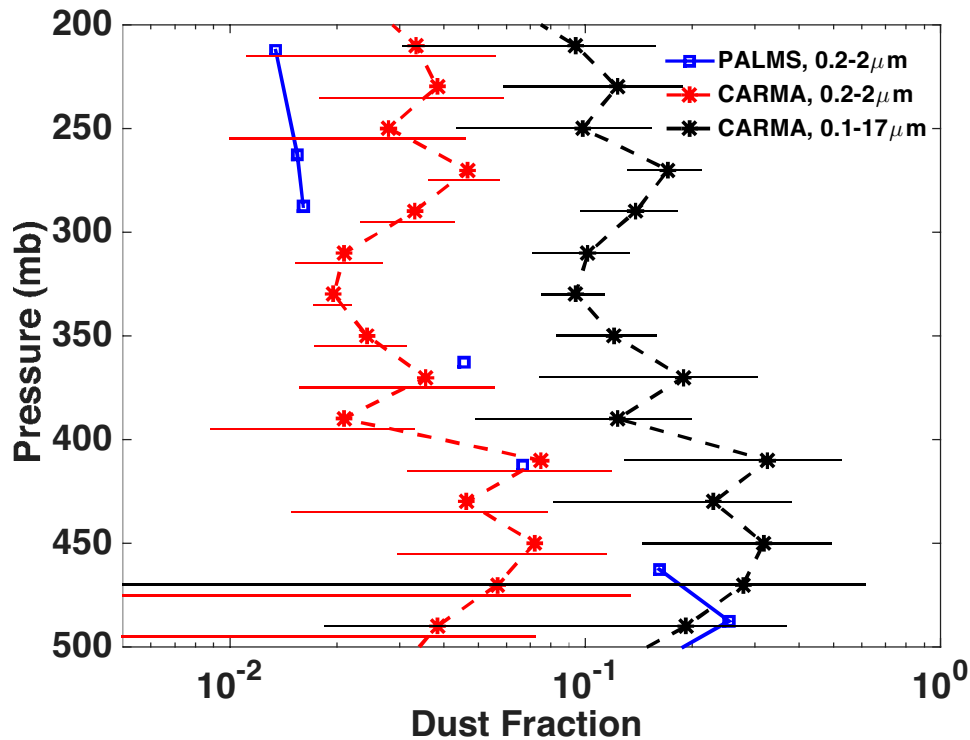240 as shown in the left panel of Figure 4.

241

242 Figure 4 (left) OA to BC mass ratio. CARMA simulations are shown in red, while

243 observations are shown in blue dashed lines. Error bars denote variability (standard

244 deviation) of observations, grey shading denotes data variability of model; (right) single

245 scattering albedo (SSA) at mid-visible wavelength simulated by CARMA (red) and

246 observed by LARGE (blue). Green lines denote calculated SSA using CRDS for dry

247 extinction coefficient and PAS for dry absorption coefficient. Black dashed lines denote

248 modeled SSA in CARMA without dust aerosols.

249   Another reason behind the lower SSA between 300 and 500 hPa is the presence of

250   dust. Figure 5 shows modeled dust mass fraction for the size range between 0.2 and 3 μm

251   in diameter (in dashed red lines); modeled mass fraction for the size range between 0.1

252   and 17 μm in diameter (in dashed black lines); in-situ PALMS data (Particle Analysis by

253   Laser Mass Spectrometry, detection limit: 0.2-2 μm in diameter, [*Murphy et al.,* 2006]) is

254   shown in blue lines. Both model and observation suggest dust mass fraction (in the size

255   range of 0.2-2 μm) is 1 to 5% in the upper troposphere (200 mb to 400 mb), while the

256   model also suggests the total dust mass fraction could be as high as 8-20%. A simulation

257   omitting dust emissions globally suggest absence of dust (dashed black lines in the right

258   panel of Figure 4) leads to a SSA increase by up to 0.05 from 400 hPa to 500 hPa.

259

260   Figure 5 Dust mass fraction: red dashed line denotes simulated in CARMA for aerosol in

261   the size range of 0.2 to 2 μm in diameter; black dashed line denotes simulated in

14

262   CARMA for aerosol in the size range of 0.1 to 17 μm in diameter; blue line denotes

263   observations from PALMS for the size range of 0.2 to 2 μm in diameter.

264   **5. Radiative Effects of Rim Fire Smoke**

265   Figure 6a shows MODIS mid-visible aerosol optical depth (AOD, Deep Blue

266   algorithm, [*Sayer et al.,* 2013]) on August 27, and Figure 6b shows simulated mid-

267   visible AOD by CARMA on August 27 with AERONET retrieved mid-visible AOD

268   shown in filled circles. Near the source region, both MODIS and AERONET see a value

269   about 1 at mid-visible, while the model predicts a value of 0.6. The underestimation is

270   likely because coarse model spatial resolution (i.e. one degree) is not sufficient to resolve

271   sub-grid fire sources. The underestimation might also due to the initial smoke emissions.

272   Downwind of the Rim fire, modeled AOD (0.3-0.6) is close to observations. The

273   simulations may be more accurate downwind due to the smoke plumes expanding

274   spatially.

275   To quantify the radiative impacts of Rim Fire smoke we conducted a control run

276   with the same settings (meteorology and initial conditions) as in the base run but without

277   black carbon and organic aerosols emitted in Rim Fire plumes. The background aerosol

278   (not from smoke) remains the same as base run. Figure 6c shows simulated clear sky net

279   radiative flux at the surface (FSNS, W m^{-2}) averaged from 20Z-22Z of August 27 (i.e.

280   13:00-15:00 local time of California) from the run with Rim Fire smoke. The simulation

281   suggests that Rim Fire smoke may prevent 4-6% of sunlight energy from reaching the

282   surface. Figure 6d illustrates the dimming efficiency (defined as FSNS difference per unit

283   mid-visible AOD, W m^{-2} per unit of AOD) calculated from the Rim Fire run and the

284   control run (20Z-22Z of August 27). In the simulations the smoke is dimming the surface

285   beneath it by 120-140 W m^{-2} per unit of mid-visible AOD. This is consistent with the

286   solar forcing efficiency of approximately -140 W m^{-2} per unit mid-visible AOD measured

287   by the BroadBand Radiometers (BBR) and the Spectrometer for Sky-Scanning, Sun

288   Tracking Atmospheric Research (4STAR) on the DC8 as it flew gradient legs into and

289   out of the smoke plume perpendicular to the smoke plume axis [*Bucholtz et al.,* 2015].

290   The measured forcing efficiency of the smoke was derived from the slope of the net solar

291   irradiance measured by the BBR versus the AOD gradient measured by 4STAR. Given

292   high SSA observed (0.95) and modeled (0.91), the surface dimming from rim fire smoke

293   is mostly due to scattering rather than absorption of soot and brown carbon in the smoke.
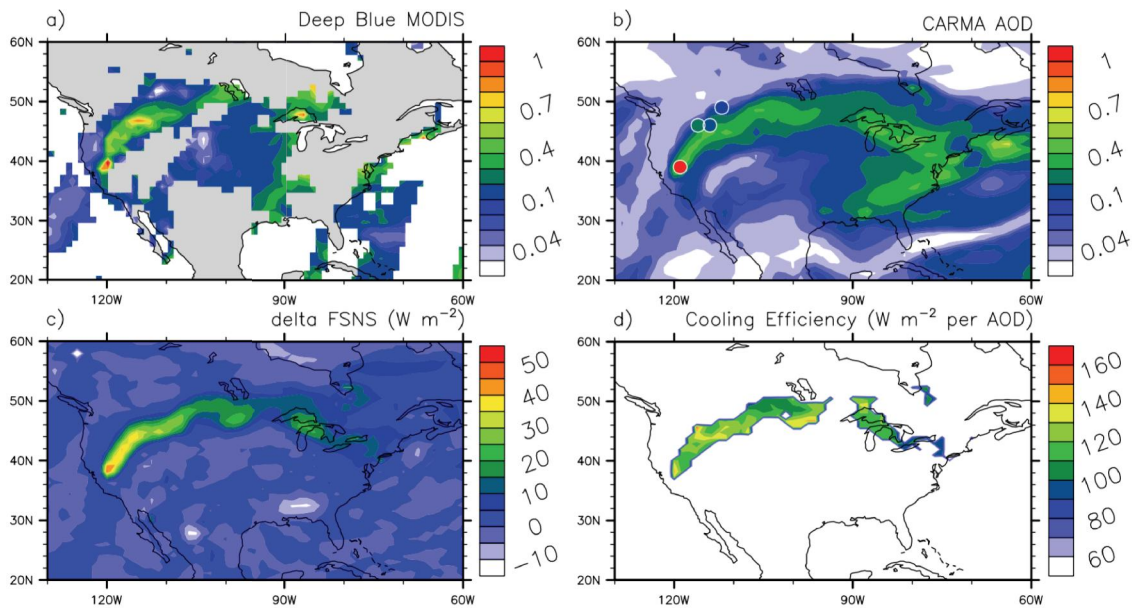

294

295   Figure 6 (a) MODIS deep blue mid-visible AOD of August 27, grey area denotes

296   no retrieval by MODIS; (b) CARMA simulated mid-visible AOD for 20Z-22Z of August

297   27; (c) Net solar flux (W m^{-2} at mid-visible) at surface simulated in CARMA for the to

298   Rim Fire smoke simulation minus the control, 20Z-22Z of August 27 (d) surface

299   dimming efficiency for rim fire smoke for 20Z-22Z of August 27: surface dimming per

300   AOD of smoke (W m^{-2} per unit of mid-visible AOD). Observation of mid-visible AOD

301 (level 2) by AERONET Sites (University of Nevada-Reno: 39N, 119W; Rimrock: 46N,

302 116W; Missoula: 46N, 114W; University of Lethbridge: 49N, 112W) close to the smoke,

303 are shown in filled cycles. AERONET observations are mostly taken between 20-22Z of

304 August 27. Due to limited observation on August 27, the AOD data of University of

305 Nevada-Reno is taken at 23 Z of August 27.

306   Figure 7 shows simulated solar heating rate (K/day) difference between runs with

307 and without smoke. Up to 1.7 K/day solar heating rate is shown between 600 and 650 hPa

308 near the source region with denser smoke, and near local noon. In the far end of the

309 smoke, the heating rate becomes noisy due to the less dense smoke and the large solar

310 zenith angles as sampling occurred late in the afternoon. Given the fact the model with 1-

311 degree resolution underestimates AOD near source region by a factor of 2-3 as shown in

312 Figure 6c, the peak solar heating rate might be several times higher than 1.7 K/day near

313 the source region. Absorption of brown carbon [*Jacobson*, 2014] is not modeled in this

314 study, but the single scatter albedo of the simulated smoke is too low.
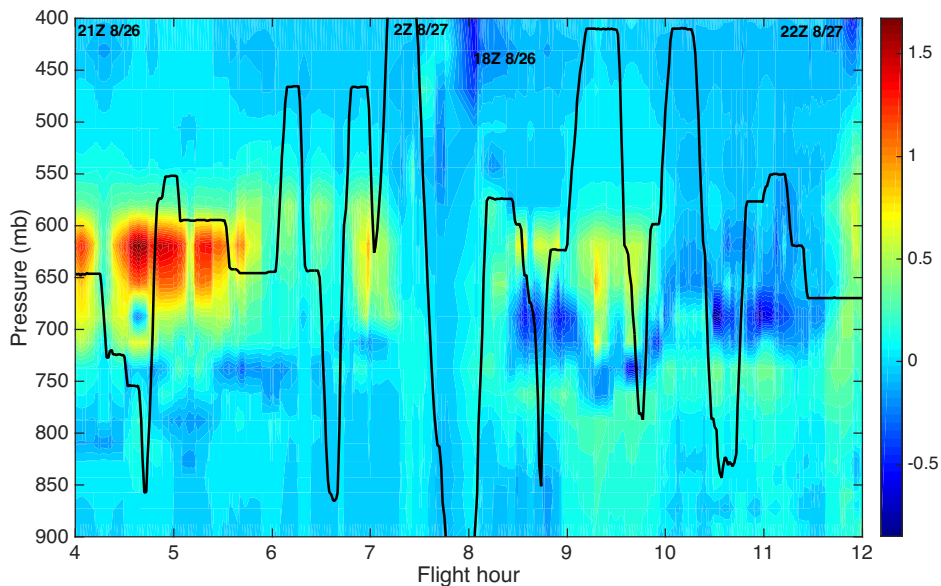

315

316   Figure 7 simulated solar heating rate (K/day) difference between runs with and without

317   Rim Fire smoke along the DC8 flight track from 21Z 8/26 to 22Z 8/27. Pressure altitudes

318   of DC8 are shown in black lines.

319   **6. Discussions and Conclusions**

320   The Rim Fire of 2013, which consumed the third largest area in California

321   history, produced a dense smoke plume. We simulate this plume for August 26 and 27,

322   when the smoke extended from the active fires in the Sierra Nevada Mountains near

323   Yosemite National Park, to southern Canada and the Great Lakes. On these days the

324   NASA DC-8 made a large number of observations of the smoke plume properties as part

325   of the SEAC4RS field program. Our simulations use the CESM1/CARMA climate model

326   with size-resolved aerosol microphysics. Our goal is to determine if a climate model,

327   with relatively coarse resolution, can correctly reproduce the smoke properties, and the

328   radiative impact of the smoke. In Table 3, we list some assumptions and limitations of the

329   model in simulating smoke's physical and optical properties. The major limitations come

330   from the uncertainties of Rim Fire emissions and the model's coarse resolution.

331   Uncertainties on injection height, initial size distribution, smoke's density and smoke's

332   aging process can affect the smoke plume mass budget, size distributions and lifetime. In

333   addition, the smoke optical properties assumed in the model are also directly related to

334   the dimming forcing calculations.

335   Table 3 Assumptions in simulating radiative impact of Rim Fire smoke

	Model Assumptions	Values or References
a	Emissions of Rim Fire Smoke	Saide et al., 2015
b	Fire Injection Height	Peterson et al., 2015
c	Fire initial size distribution	AERONET
d	Aging process of fire smoke in the model	Not Simulated
e	Model's resolution	0.9°x1.25°

f	Absorption by brown carbon	Not Simulated
g	Refractive Indices of smoke	Hess et al., 1998
h	Smoke particle shape	Core-shell structure, sphere
i	Smoke mixing state	Internal mixtures
j	Black carbon refractive indices	1.75-0.443i
k	Smoke density	Constant (1.35 g/cm^3)

336

337   Observations suggest the initial smoke aerosol concentrations peak between 550

338   and 650 hPa. Using 1-degree spatial resolution, CARMA is able to reproduce smoke OA

339   mass concentration, particle number concentration, particle surface area concentration,

340   particle volume concentration, and extinction coefficient within observed data variability,

341   though the simulated mean values for all the parameters or just extinction tend to be

342   biased low with respect to mean observed values. The simulated single scattering albedo

343   (0.9) is too low compared with observations (0.95). Surprisingly the simulated single

344   scattering albedo (SSA) at mid-visible wavelength is lower in the background air above

345   the smoke plumes than in them, due to higher simulated and observed black carbon mass

346   fraction in the aerosols above the main smoke layer and possibly due to the presence of

347   dust. Both simulations and PALMS observations suggest the dust mass fraction in the

348   upper troposphere is a few percent for particles smaller than 2 μm in diameter, while

349   CARMA simulations also suggests the dust mass fraction in upper troposphere is 8-20%

350   of total aerosol mass. Underestimates of the mean values of extinction coefficients and

351   SSA are likely related to a combination of model resolution being too low, inaccurate

352   emissions estimates, and/or injecting the emissions at a pressure that is slightly too high.

353   The simulations suggest that scattering and absorption (mostly scattering) by the

354   Rim Fire smoke reduced solar insolation at the surface at 20Z-22Z on August 27 (around

355   local noon time) by 20-50 W m^{-2}, which is roughly 4-6% of total solar radiation at the

356 surface. The simulations also suggest that forest fire smoke may reduce surface solar flux

357 with an efficiency of 120-150 W m^{-2} per unit AOD. The peak of the simulated solar

358 heating rate is 1.7 K/day, but the model may underestimate the heating rate by a factor of

359 2-3 especially near the source region because it underestimates the aerosol

360 concentrations. Following *Robock* [1991], this study suggests forest fire smoke,

361 especially on continental scales, should be taken into account when forecasting surface

362 temperature. However, weather forecasts in the mountainous region studied do not have

363 good enough signal to noise levels to reveal the impact of the smoke on the forecasts.

379   **References**

380   Amann M., I. Bertok, J. Borken-Kleefeld, J. Cofala, C. Heyes, L. Höglund-Isaksson, et

381   al. (2011), Cost effective control of air quality and greenhouse gases in Europe:

382   Modeling and policy applications. *Environmental Modelling & Software 26*:1489-

383   1501.

384   Bucholtz, A, J. Redemann, K. S. Schmidt, J. Hair, N. Wagner, and E. Reid (2015, in

385   preparation), Radiative forcing efficiencies and heating rates of forest fire smoke from

386   the 2013 RIM during SEAC4RS, for submission to *J. Geophys. Res.*

387   Chen, G., L. D. Ziemba, D. A. Chu, K. L. Thornhill et al. (2011), Observations of

388   Saharan dust microphysical and optical properties from the Eastern Atlantic during

389   NAMMA airborne field campaign, *Atmos. Chem. Phys.*, *11,* 723-740,

390   doi:10.5194/acp-11-723-2011.

391   Cubison, M. J., et al. (2011), Effects of aging on organic aerosol from open biomass

392   burning smoke in aircraft and laboratory studies, *Atmos. Chem. Phys., 11*, 12049-

393   12064, doi:10.5194/acp-11-12049-2011.

394   Darmenov, A., and A. M. da Silva (2014), The Quick Fire Emissions Dataset (QFED)

395   Documentation of versions 2.1, 2.2 and 2.4, NASA TM-2013-104606, vol. 35, 183 pp.

396   Dunlea, E. J., et al. (2009), Evolution of Asian aerosols during transpacific transport in

397   INTEX-B, Atmos. Chem. Phys., 9, 7257-7287, doi:10.5194/acp-9-7257-2009.

398   Forrister, et al. (2015), Evolution of brown carbon in wildfire plumes. *Geophys. Res.*

399   *Lett., 42*, 4623–4630. doi: 10.1002/2015GL063897.

400   Hess, M., P. Koepke and I. Schultz (1988), Optical Properties of Aerosols and Clouds:

401   The software Package OPAC. *Bull. Am. Meteorol. Soc*. 79: 831–844.

402   Iacono, M. J., J. S. Delamere, E. J. Mlawer, M. W. Shephard, S. A. Clough, and W. D.

403   Collins (2008), Radiative forcing by long-lived greenhouse gases: Calculations with

404   the AER radiative transfer models, *J. Geophys. Res.,* 113, *D13103,*

405   *doi:*10.1029/2008JD009944.

406   Jacobson, M. Z. (2014), Effects of biomass burning on climate, accounting for heat and

407   moisture fluxes, black and brown carbon, and cloud absorption effects, *J. Geophys.*

408   *Res. Atmos., 119*, 8980–9002, doi:10.1002/2014JD021861.

409   Jolleys, M.D., et al. (2012), Characterizing the Aging of Biomass Burning Organic

410   Aerosol Using Mixing Ratios - a Meta-analysis of Four Regions. *Environmental*

411   *Science & Technology, 46*, 13093–13102, DOI: 10.1021/es302386v.

412   Justin M. Langridge, M. S. Richardson, D. Lack, D. Law and D. M. Murphy (2011),

413   Aircraft Instrument for Comprehensive Characterization of Aerosol Optical Properties,

414   Part I: Wavelength-Dependent Optical Extinction and Its Relative Humidity

415   Dependence Measured Using Cavity Ringdown Spectroscopy, *Aerosol Science and*

416   *Technology*, *45:11*, 1305-1318, DOI: 10.1080/02786826.2011.592745.

417   Langridge, J. M., et al. (2011), Aircraft instrument for comprehensive characterization of

418   aerosol optical properties, part I: Wavelength‐dependent optical extinction and its

419   relative humidity dependence measured using cavity ringdown spectroscopy, *Aerosol*

420   *Sci. Technol., 45*, 1305–1318, doi:10.1080/02786826.2011.592745

421   Langridge, J. M., et al. (2013) Limitations of the Photoacoustic Technique for Aerosol

422   Absorption Measurement at High Relative Humidity, *Aerosol Sci. Technol.*, *47*, 1163-

423   1173, DOI: 10.1080/02786826.2013.827324.

424   Murphy, D. M., et al. (2006), Single-particle mass spectrometry of tropospheric aerosol

425   particles, *Journal of Geophysical Research-Atmospheres*, *111*(D23),

426   doi:10.1029/2006jd007340.

427   Peterson, D. A., E. J. Hyer, J. R. Campbell, M. D. Fromm, J. W. Hair, C. F. Butler, and

428   M. A. Fenn (2014), The 2013 Rim Fire: Implications for predicting extreme fire

429   spread, pyroconvection, and smoke emissions, Bull. Am. Meteorol. Soc., 96, 229–247,

430   doi:10.1175/bams-d-14-00060.1.

431   Rienecker, M. M., et al. (2011), Merra: nasa's modern-era retrospective analysis for

432   research and applications. *J. Climate*, *24*, 3624–3648, doi:

433   http://dx.doi.org/10.1175/JCLI-D-11-00015.1.

434   Robock, A. (1988), Enhancement of Surface Cooling Due to Forest Fire Smoke, *Science,*

435   *242*, 911-913, *doi:* 10.1126/science.242.4880.911.

436   Robock, A. *(*1991*),* Surface cooling due to forest fire smoke*,* J. *Geophys. Res., 96(*D11*),*

437   20869–20878*, doi:*10.1029/91JD02043*.*

438   Saide, P. E.*, et al. (*2015*),* Revealing important nocturnal and day-to-day variations in fire

439   smoke emissions through a multiplatform inversion*, Geophys. Res. Lett., 42,*

440   *doi:*10.1002/2015GL063737*.*

441   Sayer, A. M., N. C. Hsu, C. Bettenhausen, and M.-J. Jeong (2013), Validation and

442   uncertainty estimates for MODIS Collection 6 "Deep Blue" aerosol data, *J. Geophys.*

443   *Res. Atmos., 118*, 7864–7872, doi:10.1002/jgrd.50600.

444   Schwarz, J. P.*,* B. H. Samset*,* A. E. Perring*,* J. R. Spackman*,* R. S. Gao*,* P. Stier*,* M.

445   Schulz*,* F. L. Moore*,* E. A. Ray*, and* D. W. Fahey (2013), Global-scale seasonally

446   resolved black carbon vertical profiles over the Pacific*, Geophys. Res. Lett.,* 40*,* 5542–

447   5547*, doi:*10.1002/2013GL057775*.*

448   Toon, O. B., R. P. Turco, D. Westphal, R. Malone, and M. S. Liu (1988), A

449   Multidimensional model for aerosols - description of computational analogs, *Journal*

450   *of the Atmospheric Sciences*, *45*(15), doi:10.1175/1520-0469(1988).

451   Toon, O. B., et al. (2016), Planning, implementation, and scientific goals of the Studies of

452   Emissions and Atmospheric Composition, Clouds and Climate Coupling by Regional

453   Surveys (SEAC4RS) field mission, *J. Geophys. Res. Atmos*., *121*,

454   doi:10.1002/2015JD024297.

455   Westphal, D. L., and O. B. Toon (1991), Simulations of microphysical, radiative, and

456   dynamical processes in a continental-scale forest fire smoke plume, *J. Geophys.*

457   *Res., 96*(D12), 22379–22400 doi:10.1029/91JD01956.

458   Yu, P., O. B. Toon, C. G. Bardeen, M. J. Mills, T. Fan, J. M. English, and R. R.

459   Neely (2015a),Evaluations of tropospheric aerosol properties simulated by the

460   community earth system model with a sectional aerosol microphysics scheme, *J. Adv.*

461   *Model. Earth Syst., 7*, 865–914, doi:10.1002/2014MS000421.

462   Yu, P., O. B. Toon, R. R. Neely, B. G. Martinsson, and C. A. M. Brenninkmeijer

463   (2015b), Composition and physical properties of the Asian Tropopause Aerosol Layer

464   and the North American Tropospheric Aerosol Layer. *Geophys. Res. Lett., 42,* 2540–

465   2546. doi: 10.1002/2015GL063181.

466   Ziemba L. D.*, et al. (*2013*),* Airborne observations of aerosol extinction by in situ and

467   remote-sensing techniques: Evaluation of particle hygroscopicity*, Geophys. Res. Lett.,*

468   *40,* 417–422*, doi:*<u>10.1029/2012GL054428</u>*.*